



Image-based computer modeling assessment of microwave ablation for treatment of adrenal tumors

Sebek, J., Cappiello, G., Rahmani, G., Zeinali, N., Keating, M., Fayemiwo, M., Harkin, J., McDaid, L.J., Gardiner, B., Sheppard, D., Senanayake, R., Gurnell, M., O'Halloran, M., Denny, C., & Prakash, P. (2022). Image-based computer modeling assessment of microwave ablation for treatment of adrenal tumors. *International Journal of Hyperthermia*, 39(1), 1264-1275. <https://doi.org/10.1080/02656736.2022.2125590>

[Link to publication record in Ulster University Research Portal](#)

Published in:
International Journal of Hyperthermia

Publication Status:
Published: 22/09/2022

DOI:
[10.1080/02656736.2022.2125590](https://doi.org/10.1080/02656736.2022.2125590)

Document Version
Publisher's PDF, also known as Version of record

General rights
Copyright for the publications made accessible via Ulster University's Research Portal is retained by the author(s) and / or other copyright owners and it is a condition of accessing these publications that users recognise and abide by the legal requirements associated with these rights.

Take down policy
The Research Portal is Ulster University's institutional repository that provides access to Ulster's research outputs. Every effort has been made to ensure that content in the Research Portal does not infringe any person's rights, or applicable UK laws. If you discover content in the Research Portal that you believe breaches copyright or violates any law, please contact pure-support@ulster.ac.uk.

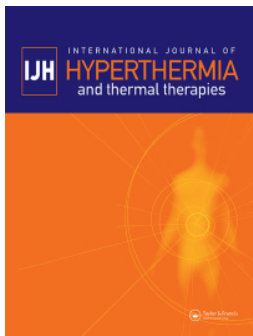


Image-based computer modeling assessment of microwave ablation for treatment of adrenal tumors

Jan Sebek, Grazia Cappiello, George Rahmani, Nooshin Zeinali, Muireann Keating, Michael Fayemiwo, Jim Harkin, Liam McDaid, Bryan Gardiner, Declan Sheppard, Russell Senanayake, Mark Gurnell, Martin O'Halloran, M. Conall Dennedy & Punit Prakash

To cite this article: Jan Sebek, Grazia Cappiello, George Rahmani, Nooshin Zeinali, Muireann Keating, Michael Fayemiwo, Jim Harkin, Liam McDaid, Bryan Gardiner, Declan Sheppard, Russell Senanayake, Mark Gurnell, Martin O'Halloran, M. Conall Dennedy & Punit Prakash (2022) Image-based computer modeling assessment of microwave ablation for treatment of adrenal tumors, International Journal of Hyperthermia, 39:1, 1264-1275, DOI: [10.1080/02656736.2022.2125590](https://doi.org/10.1080/02656736.2022.2125590)

To link to this article: <https://doi.org/10.1080/02656736.2022.2125590>



© 2022 The Author(s). Published with license by Taylor & Francis Group, LLC



[View supplementary material](#)



Published online: 22 Sep 2022.



[Submit your article to this journal](#)



Article views: 158






[View related articles](#)



[View Crossmark data](#)

Image-based computer modeling assessment of microwave ablation for treatment of adrenal tumors

Jan Sebek^a , Grazia Cappiello^b, George Rahmani^c, Nooshin Zeinali^a, Muireann Keating^d, Michael Fayemiwo^e, Jim Harkin^e, Liam McDaid^e, Bryan Gardiner^e, Declan Sheppard^c, Russell Senanayake^f, Mark Gurnell^f , Martin O'Halloran^b, M. Conall Dennedy^d and Punit Prakash^a 

^aMike Wiegiers Department of Electrical and Computer Engineering, Kansas State University, Manhattan, KS, USA; ^bTranslational Medical Devices Lab, National University of Ireland, Galway, Republic of Ireland; ^cDepartment of Radiology, Galway University Hospitals, Galway, Republic of Ireland; ^dSchool of Medicine, National University of Ireland, Galway, Republic of Ireland; ^eSchool of Computing, Engineering, and Intelligent Systems, Ulster University, Londonderry, Northern Ireland; ^fInstitute of Metabolic Science, University of Cambridge, Cambridge, UK

ABSTRACT

Purpose: To assess the feasibility of delivering microwave ablation for targeted treatment of aldosterone-producing adenomas using image-based computational models.

Methods: We curated an anonymized dataset of diagnostic ¹¹C-metomidate PET/CT images of 14 patients with aldosterone-producing adenomas (APA). A semi-automated approach was developed to segment the APA, adrenal gland, and adjacent organs within 2 cm of the APA boundary. The segmented volumes were used to implement patient-specific 3D electromagnetic-bioheat transfer models of microwave ablation with a 2.45 GHz directional microwave ablation applicator. Ablation profiles were quantitatively assessed based on the extent of the APA target encompassed by an ablative thermal dose, while limiting thermal damage to the adjacent normal adrenal tissue and sensitive critical structures.

Results: Across the 14 patients, adrenal tumor volumes ranged between 393 mm³ and 2,395 mm³. On average, 70% of the adrenal tumor volumes received an ablative thermal dose of 240CEM43, while limiting thermal damage to non-target structures, and thermally sparing 83.5–96.4% of normal adrenal gland. Average ablation duration was 293 s (range: 60–600 s). Simulations indicated coverage of the APA with an ablative dose was limited when the axis of the ablation applicator was not well aligned with the major axis of the targeted APA.

Conclusions: Image-based computational models demonstrate the potential for delivering microwave ablation to APA targets within the adrenal gland, while limiting thermal damage to surrounding non-target structures.

ARTICLE HISTORY

Received 16 June 2022
Revised 29 August 2022
Accepted 12 September 2022



KEYWORDS

Image-based modeling;
microwave ablation;
aldosterone-producing
adenomas; patient-specific
modeling; thermal damage

Introduction

Primary aldosteronism (PA) is the principal cause of secondary hypertension and accounts for 5–12% of all hypertension worldwide [1–4]. PA is characterized by dysregulated aldosterone secretion from unilateral or bilateral aldosterone-producing adenoma (APA), aldosterone-producing macronodules (MAPN)/micronodules (MAPM), or aldosterone-producing diffuse hyperplasia (APDH). Primary hyperaldosteronism is associated with greater levels of cardiovascular and renovascular co-morbidities when compared to matched primary hypertension, including atrial fibrillation, ventricular hypertrophy, hypokalemia, and cerebrovascular ischemic events [5,6]. Hyperaldosteronism may arise from one (unilateral PA) or both (bilateral PA) adrenal glands and distinguishing unilateral from bilateral disease (lateralization) is the key step

following diagnosis to determining the most appropriate therapeutic approach to resolving PA. The gold-standard lateralization procedure is adrenal vein sampling (AVS), although functional imaging using ¹¹C Metomidate PET/CT has demonstrated high specificity in not just lateralizing disease, but also localizing offending nodules within the gland [7]. The current recommended definitive management for patients affected by unilateral APA or APCC is adrenalectomy – i.e., complete surgical resection of a single adrenal, while in patients with bilateral disease pharmacological therapy is the treatment of choice with primacy given to mineralocorticoid receptor antagonist (MRA) therapy. Bilateral adrenalectomy is not indicated for patients with bilateral disease given unavoidable and unacceptable adrenocortical insufficiency arising from this approach. Pharmacotherapy with MRAs is

CONTACT Punit Prakash  prakashp@ksu.edu  Mike Wiegiers Department of Electrical and Computer Engineering, Kansas State University, 3078 Engineering Hall, 1701D Platt St, Manhattan, KS 66506, USA

 Supplemental data for this article is available online at <https://doi.org/10.1080/02656736.2022.2125590>.

© 2022 The Author(s). Published with license by Taylor & Francis Group, LLC

This is an Open Access article distributed under the terms of the Creative Commons Attribution License (<http://creativecommons.org/licenses/by/4.0/>), which permits unrestricted use, distribution, and reproduction in any medium, provided the original work is properly cited.

also not always well tolerated in males [8,9] due to feminizing off-target effects at the androgen receptor. While in women of reproductive age, MRA carry teratogenic potential to the fetus.

Image-guided thermal ablation may provide a minimally-invasive approach for targeted destruction of aldosterone producing lesions which have been located in one or both adrenal glands. Specific, targeted delivery of thermal ablation could also thermally spare adjacent normally functioning adrenal tissue, while avoiding damage to adjacent sensitive structures [10]. Thermal ablation may therefore present a non-pharmacologic treatment for patients with PA underpinned by both unilateral and bilateral disease.

In using an adrenal-sparing, targeted approach to unilateral or bilateral PA, it is necessary to localize the offending aldosterone producing lesions within each adrenal gland in order to plan effective targeting. ^{11}C -metomidate PET/CT imaging provides a modality for localizing functioning, aldosterone producing adrenal lesions, with PET imaging overlaid on anatomic detail available through CT imaging.

Both radiofrequency [10] and microwave ablation (MWA) have been successfully applied to treat unilateral functioning adrenal adenomas causing both PA and hypercortisolism ($\leq 20\text{ mm}$) [11–13]. These approaches have demonstrated success in obtaining complete adenoma thermal ablative coverage during a single treatment, achieving biochemical and complete cure comparable to that achieved with adrenalectomy [13–15]. Additionally, we have previously demonstrated in an animal model, the feasibility of bilateral subtotal ablation within the adrenal gland to achieve ablation zones of $\sim 1\text{ cm}^3$, while preserving adjacent adrenal cortex and normal post-procedural adrenocortical function [16].

Targetable aldosterone producing lesions are typically between 300 and 2500 mm^3 in diameter. Currently available MWA devices are well suited to creating near-spherical ablation zones $>2\text{ cm}$ in diameter (volume: $>4.2\text{ cm}^3$), due to the relatively long wavelength at the commonly used frequencies of 2.45 GHz and 915 MHz. These probes are not ideally suited to creation of smaller ablation zones. Dielectric contrast between peri-adrenal fat and the adrenal cortex can also constrain microwave power toward the gland [17]. Finally, present MWA probes typically require penetration into the offending lesion in order to deliver radiation. We have developed MWA devices with directional control of radiation pattern that may offer the opportunity to target smaller lesions, such as aldosterone producing lesions without requiring direct penetration into the adrenal gland and which can be directed away from peri-adrenal fat when applying ablation [18–20].

We used directional probes and specifically applied this approach during *in vivo* porcine studies which demonstrated therapeutic potential for subtotal, targeted bilateral adrenal ablation in this context, when the MWA device was positioned during laparotomy [16]. However, this pre-clinical study was limited by the fact that MWA was undertaken in normal porcine adrenal gland as there are no current large animal models of adrenal nodules, and did not therefore consider the location of potential adrenal nodules. Moreover, the MWA probe

placement was performed during laparotomy, rather than using a minimally invasive approach and therefore organs adjacent to the adrenal could be reflected away from the field of radiation to avoid damage. Computational models provide an approach to overcome these limitations, prior to application in the *in vivo* model and can investigate the potential to deliver effective conformal thermal ablation to site-specific targets, within a simulated patient environment derived from clinical imaging [21–24].

The objective of this study was to characterize microwave ablation profiles within APA targets using computational models derived from representative clinical imaging datasets. Coupled electromagnetic-bioheat transfer simulations were implemented incorporating the adrenal gland, APAs, and surrounding tissue structures, as informed by a dataset of ^{11}C -metomidate PET/CT images from 14 patients. Ablation profiles were quantitatively assessed based on the extent of the APA target encompassed by an ablative thermal dose, while limiting thermal damage to the adjacent normal adrenal tissue and avoiding damage to sensitive critical structures. The results provide insight into the range of APA targets that can be ablated with 2.45 GHz directional microwave ablation applicators considered in this study.

Methods

Patient imaging dataset

Clinical evaluation was performed on patients attending a resistant/young hypertension clinic at Galway University Hospital between 2014 and 2018, who met the following criteria: (i) diagnosis of PA, (ii) had undergone lateralization with AVS, ^{11}C -metomidate PET/CT or both, (iii) had outcome data for >6 months following adrenalectomy or commencement of MRA (for bilateral disease or those awaiting adrenalectomy). Each patient ($n = 14$) had been referred for work-up and management of hypertension from primary or secondary care for the following reasons: (i) young age of hypertension onset (<40 years), (ii) hypertension complicated by cardiovascular disease or hypokalemia, (iii) difficulty in controlling hypertension on three or more anti-hypertensive medications. Approval was received from the Research Ethics Committee at Galway University Hospital (GUH) and data were used with their informed consent.

Screening and diagnosis of primary aldosteronism

All patients underwent standardized screening and diagnostic approach for endocrine hypertension. PA was diagnosed according to Endocrine Society Guidelines [25]. Screening used a mid-morning aldosterone renin ratio (ARR) following two hours of ambulation with each patient seated for 15 min prior to venesection. Washout of interfering medications was performed on all patients. Confirmatory testing was performed using the seated saline infusion test (SSIT) [26,27]. Blood pressure was controlled during screening and diagnosis using a combination of doxazosin and a calcium channel antagonist. Potassium was corrected where necessary in

advance of all blood sampling. Threshold ARR and aldosterone values are reported according to locally determined laboratory reference ranges: suppressed plasma renin activity (PRA) was accepted at values <1.0 ng/mL/h, and direct renin concentrations (DRC) <9.0 mIU/L; raised aldosterone renin ratio (ARR) was accepted at values >800 pmol/L:ng/mL/h when calculated using the PRA and >35 pmol:mIU when using the DRC.

Lateralization

Upon diagnosis of PA, each patient underwent 3 mm slice CT scan of the adrenal glands (pre-contrast and venous phases). Lateralization was assessed using adrenal vein sampling (AVS) and/or ^{11}C -Metomidate PET/CT. AVS was the lateralization modality of choice and was considered for all patients. ^{11}C -Metomidate PET/CT was chosen as an adjunct or alternative lateralization modality under the following circumstances: (i) prior failed AVS; (ii) unable to stop interfering medications for diagnosis or lateralization; (iii) patient refusal of AVS; (iv) equivocal lateralization using AVS (defined as a LI between 2 and 4 using ACTH-unstimulated AVS); (iv) discordance between CT appearance of the adrenals and the LI on AVS.

^{11}C -Metomidate PET/CT

^{11}C -Metomidate PET/CT was performed at Addenbrooke's Hospital Cambridge. All patients were pretreated with 0.5 mg dexamethasone 6 hourly for 72 h prior to scanning [28,29]. ^{11}C -Metomidate was manufactured on site in compliance with good manufacturing practice using a GE Medical Systems PETtrace cyclotron (Milwaukee, WI), as previously described [29].

PET-CT was performed on a GE Discovery 690 PET-CT scanner (GE Medical Systems). Noncontrast CT images were acquired over the adrenals (140 kV, 64 mA, slice width 3.75 mm). After an iv injection of ^{11}C -metomidate (150–500 MBq), dynamic PET images were acquired for 45 min. Attenuation and decay-corrected images were converted to SUV maps through division by (injected activity per patient weight). The maximum standardized uptake values (SUV_{max}) over regions of interest were determined for 10-min static images starting 35 min after the injection. Images were analyzed and reported in line with previously published standards [28]. Lateralization of ^{11}C -Metomidate PET/CT was interpreted as an SUV_{max} ratio of 1.25 to the lateralizing side [28], or focal uptake of metomidate within a lateralizing nodule.

Image-based computational model of microwave ablation of APA

Computational models of thermal ablation are widely used for guiding the design, optimization, and assessment of candidate devices in a range of tissue types [30]. During early-stage design of devices, computational models often employ simplified characterization of tissue as homogeneous or

layered media [18,31–35]. More advanced models considering anatomy of targeted tissue regions and adjacent organs, informed by anonymized and de-identified medical imaging data, are highly informative for assessing the impact of device design parameters and energy delivery settings on thermal dose coverage of targeted tissues, as well as off-target heating of surrounding structures [21,22,36,37]. Such models are also informative for assessing the impact of the trajectory/approach for delivering needle- or catheter-based ablation devices on predicted thermal profiles in targeted and non-target tissue. In the present study, we generated computational models for assessing microwave ablation of adrenal APAs based off ^{11}C -metomidate PET/CT images.

Segmentation of the target nodule and surrounding tissue structures

A two-step process was used to localize and then segment APAs within the adrenal gland. First, the APA location was determined as the region within the adrenal gland with maximum intensity in PET images. Then, the co-registered CT image was used to manually segment irregular shapes (i.e., the APA) within the respective adrenal gland. Furthermore, we segmented any organ or large blood vessel, which was located within 2 cm from the tumor boundary. Other relevant tissue types were segmented with the use of semi-automatic approach based on two steps. In the first step, we manually placed multiple points along the target boundary. In the second step, a closed curve was assembled by automatic connection of points from the first step by finding a path of least pixel intensity difference between two neighboring points. This procedure was repeated for each axial slice of CT image. Furthermore, we have chosen the positions of microwave applicator for each case by defining two points along the applicator axis. The first point was selected on the outer surface of APA near its center of mass, where we intended to achieve the most intense heating. The position of applicator was further refined by moving it away from any organ with the risk of unacceptable collateral damage. The second point was chosen between the ribs such that the applicator followed direction of feasible introduction to the considered position and its axis avoided any organs, therefore simulating clinical approach. All segmented volumes and proposed applicator positions were reviewed, and either accepted or modified, by a board-certified radiologist (G.R.) to yield a final set of verified segmentations which were used to construct computational models.

Computational models for assessment of transient thermal profiles in tissue

We employed a coupled 3D electromagnetic-bioheat transfer models for simulating thermal profiles created by a water-cooled 2.45 GHz directional microwave ablation applicator, which consisted of 6 mm long s-shaped monopole at the radiating tip of UT34 coaxial cable inside stainless-steel tube with hemi-cylindrical reflector according to our previous study [18]. This computational modeling approach has previously been validated against volumetric MRI thermometry

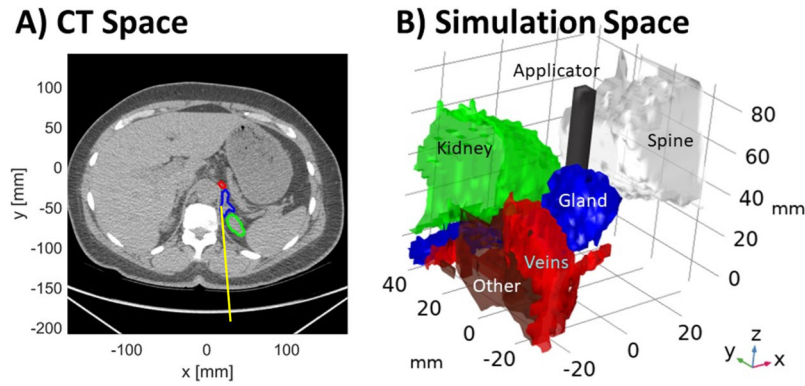


Figure 1. (A) Example CT image illustrating MWA applicator insertion path, adrenal gland, and adjacent structures. (B) computational model representing this case constructed from the segmented tissue regions and application position.

data in *ex vivo* tissue [38]. Briefly, the finite element method (FEM) was used to discretize and solve the coupled electromagnetic – heat transfer problem at time points as determined by the Backward Differentiation Formula (BDF) solver with maximum order 2 and relative tolerance 0.0005 to aid the computation convergence. The simulation space consisted of cylinder with diameter 6 cm and height 8 cm, which was centered around the ablation applicator. Tissue regions and organs segmented as described in the prior section were imported into the simulation space (see Figure 1). Regions within the simulation space not assigned to one of the organs/tissues specified at Table 1, were assigned properties of muscle tissue to approximate general soft tissue. Simulations were run for up to 10 min, with an applied power level of 80 W at the coaxial feedline input port.

A non-uniform mesh with tetrahedral elements was employed, with mesh density highest around the input port of applicator (maximal tetrahedral element edge length = 0.2 mm). The element size was allowed to grow up to 0.5 mm around the applicator shaft, and 1 mm around various tissue boundaries. The mesh was coarsest in the regions furthest away from antenna and tissue boundaries with a maximum element edge length of 4 mm. The maximum rate of mesh element growth was set to 1.5.

At each time step as taken by the solver, the time harmonic Helmholtz electromagnetic wave equation was solved to determine the spatial distribution of the electric field

$$\nabla^2 \mathbf{E} + \beta_0^2 \left(\epsilon_r - \frac{j\sigma}{\omega\epsilon_0} \right) \mathbf{E} = 0, \quad (1)$$

where \mathbf{E} is the electric field [V/m], β_0 is the wavenumber in free space [1/m], ϵ_r is relative permittivity [–], σ is electric conductivity [S/m], ω is the angular frequency [rad/s] and ϵ_0 is the permittivity of free space [F/m]. The time-averaged microwave power absorbed, Q_{mw} , was calculated with:

$$Q_{mw} = \frac{1}{2} \sigma |\mathbf{E}|^2 \quad (2)$$

Transient temperature profiles were calculated using Pennes' bioheat transfer equation [39]

$$\rho c(T) \frac{\partial T}{\partial t} = \nabla \cdot k(T) \nabla T + Q_{mw} - m_{bl}(T) c_{bl}(T - T_{bl}) \quad (3)$$

where $\rho c(T)$ is volumetric heat capacity [J/m³/K], T is temperature [K], $k(T)$ is the thermal conductivity [W/m/K], $m_{bl}(T)$ is the blood mass perfusion rate [kg/m³/s], c_{bl} is the specific heat capacity of blood [J/kg/K], and T_{bl} is the blood temperature [K]. Furthermore, the heatsink associated with large vessels like the aorta or vena cava was approximated by omitting the electromagnetic heat source from such volumes (i.e., setting $Q_{mw} = 0$ W/m³ in these volumes) and assigning a large blood perfusion value as listed in Table 1. Tissue dielectric and thermal properties are temperature-dependent; nominal values of tissue physical properties at physiologic temperature (37 °C) used in our simulations are listed in Table 1.

At each time step of the computation, tissue properties were updated according to their temperature dependencies. Expressions for the normalized values (unit value at physiologic temperature) of temperature dependent tissue properties for each tissue type are presented in the accompanying Supplementary Materials (Table SI). Expressions for dielectric and thermal temperature dependencies were adopted from [43,44] and from [45] respectively. Temperature dependency of relative permittivity, effective conductivity, and thermal conductivity was piecewise linear function, while for volumetric heat capacity and blood perfusion coefficient, we utilized piecewise constant function. All functions were smoothed to have a continuous second derivative, with the absolute size of transition zone in the range 5–20 °C.

In all regions of the simulation domain, the initial temperature was set to physiologic temperature 37 °C. To speed-up convergence of the electric field solver, the initial value of the electric field intensity was set to 1000 V/m (isotropic) in all tissue regions. At the simulation boundaries, we applied first order scattering boundary condition approximating the Sommerfeld radiation condition [18] for a spherical wave and a thermal insulation boundary condition. Additionally, we set perfect electric conductor boundary condition to all surfaces of metallic parts of the microwave applicator. Finally, we applied a convective heat-flux boundary condition (heat-flux coefficient 200 W/m²/K and external temperature 20 °C) at the outer surface of the applicator shaft to approximate the cooling effects of circulating water through the applicator.

Table 1. Tissue biophysical properties employed in FEM simulation at 2.45 GHz.

Tissue	Tissue property [40–42]				
	Relative permittivity ϵ_r [–]	Electrical conductivity σ [S/m]	Volumetric heat capacity ρc [J/m ³ /K]	Thermal conductivity k [W/m/K]	Blood perfusion rate m_{bl} [kg/m ³ /s]
Adrenal gland	58	1.07	3.61×10^6	0.44	26.8
Adrenal tumor (APA)	32.4	1.2	3.82×10^6	0.52	26.8
Fat	10.8	1.75	2.14×10^6	0.52	0.6
Kidney	52.7	2.43	4.01×10^6	0.53	69.7
Blood vessel*	58.3	2.54	3.79×10^6	0.52	12.5
Stomach	62.2	2.21	4.01×10^6	0.53	8.5
Liver	43	1.69	3.82×10^6	0.52	15.8
Spine**	11.4	0.394	2.68×10^6	0.32	0.18
Spleen	52.4	2.24	3.92×10^6	0.53	28.6
Small Intestine	53.9	2.04	3.76×10^6	0.54	14.2
Muscle	44	1.75	3.82×10^6	0.52	0.55

*Aorta, vena cava, other large vein. **Modeled as cortical bone.

Assessment of thermal damage in targeted APAs and non-targets

The thermal damage induced in tissue following ablation was estimated using the Sapareto-Dewey thermal dose method [46]:

$$CEM43(T, t) = \sum_{i=1}^N R_{CEM}^{43-T_i} \cdot t_i, \quad (4)$$

where $CEM43(T, t)$ are cumulative equivalent minutes at 43 °C [min], T_i is spatial temperature profile observed at i -th time-step with duration t_i , and N is total number of time steps. Previously established threshold value of 240 CEM43 was chosen as an estimate of the ablation boundary [47–50]. For each case, we assessed the fraction [%] of the APA target volume heated to an ablative threshold (i.e., 240 CEM43), as well as the volume [mm³] of non-target tissue regions heated to an ablative thermal dose. Since APAs are benign tumors, we did not consider ablating a margin of normal tissue circumscribing the targeted APA, as is desired for ablation of malignant disease [51]. Since a goal of ablation procedures for treating PA is to maximally preserve normal adrenal tissue, we also computed the fraction [%] of the adrenal gland excluding the APA that was heated to an ablative thermal dose.

Ablation simulations were run for up to 10 min, unless one of two events triggered termination of the simulation at an earlier timepoint. The first triggering event was based of an assessment of the rate of growth of the ablation; if after the first minute of heating, the rate of growth of the ablation zone between in consecutive timesteps dropped below 1% of the rate of ablation zone growth during the first minute of ablation, the ablation zone was considered as saturated, and the simulation was terminated. The second triggering event was damage to non-target structures exceeding pre-defined acceptable thresholds. The table of threshold volumes for acceptable collateral damage is provided in Table 2.

Values of acceptable damage thresholds in Table 2 were chosen based on consultation with board certified radiologists (G.R. and D.S.). Additionally, simulated ablations were terminated if >60% of the volume of the normal adrenal gland regions were heated above the ablative threshold. For critical structures such as the aorta and vena cava, where no

Table 2. Acceptable volumes of collateral damage in different organs.

Organ	V [mm ³]
Spine	2000
Liver	1000
Stomach	0
Kidney	1000
Spleen	0
Small veins	1000
Aorta*	0
Vena Cava*	0
Other*	0

*A value of 0 mm³ indicates no ablation to the structures was considered acceptable.

damage can be tolerated, simulations were terminated when a non-zero value of ablation volume was observed.

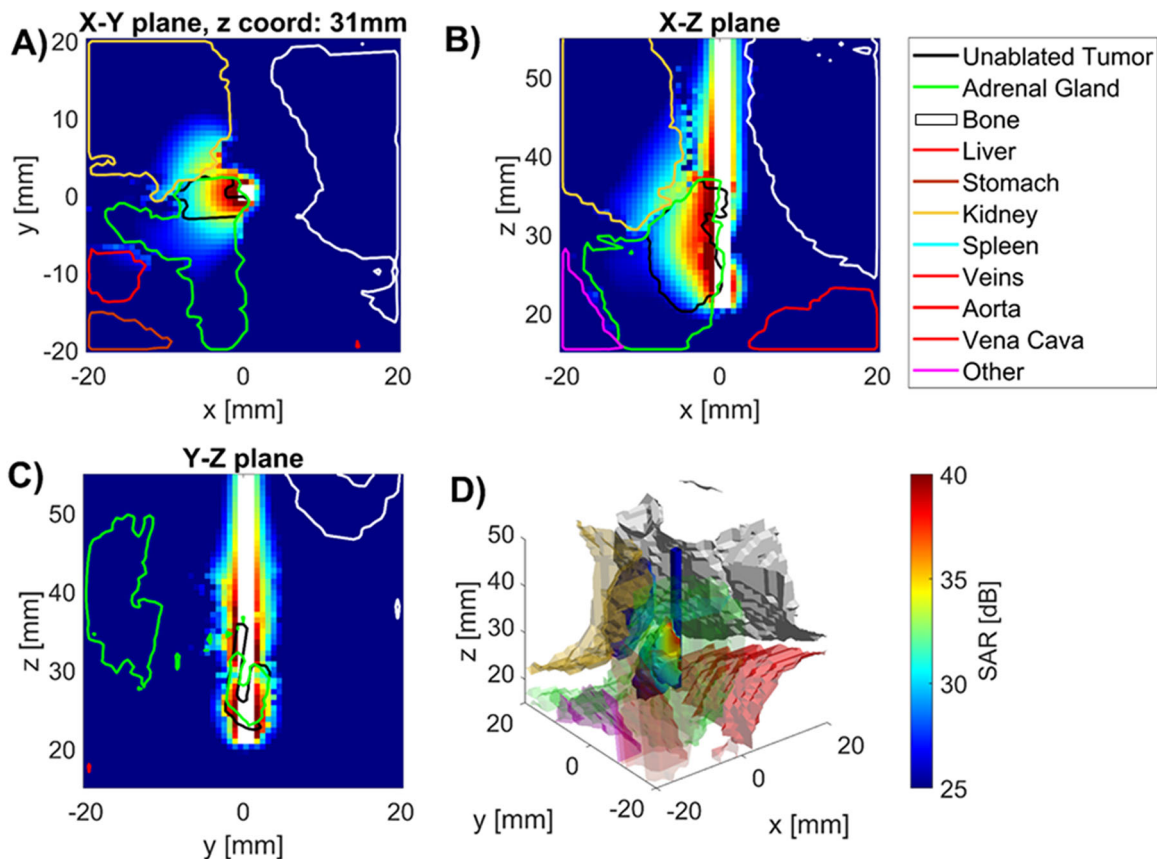
Results

Image-based computer models were generated from PET/CT imaging datasets for a total of 14 patients. Table 3 and Table SII (Supplementary Materials) provide a summary of target APA nodule characteristics, criteria for terminating ablation simulations, duration of simulated ablations, total volume of ablated tissue, fraction of APA heated to an ablative thermal dose, and thermally affected organs/tissue regions for ablations estimated by 240 CEM43 and 55 °C respectively. APA volumes considered in this study were of volumes ranging between 393 mm³ and 2395 mm³. Cumulative volumes of all tissue regions heated to an ablative thermal dose ranged between 981 mm³ and 11,328 mm³. Across all 14 cases, the average fraction of the target volume receiving an ablative thermal dose was 70%. In 8/14 cases, simulations indicated >70% (range: 71.3–93.7%) of the targeted volume would be heated to ablative doses. Of the eight cases where >70% of the APA received an ablative thermal dose, four simulations were terminated due to the saturation of ablation zone growth criterion, two simulations were terminated due to thermal damage to surrounding structures, and the remaining two simulations extended for the full 600 s ablation.

Figure 2 illustrates the specific absorption rate (SAR) profile in tissue regions surrounding the MWA applicator for case 1. The SAR profiles are shown in three orthogonal planes, as well as overlaid on 3D renderings of the targeted tumor, adrenal gland, and surrounding structures. These data

Table 3. Summary data for 14 simulated APA microwave ablation cases and ablation boundary estimated by threshold of 240 CEM43.

Case	APA volume [mm ³]	Stopping criterion	Ablation time [s]	Total volume of ablated tissue. [mm ³]	Fraction of APA ablated [%]	Short axis [mm]	Long axis [mm]	Height [mm]	Thermally affected organs/regions
1	650	Saturation	270	3,877	90	16.8	17.5	26.6	Gland: 9.7% Kidney: 242 mm ³
2	393	Organ at risk	90	1,484	58	11.9	13.3	21.0	Gland: 13.9% Kidney: 324 mm ³
3	628	Saturation	240	3,701	94	23.1	21.7	26.6	Gland: 12.8% Veins: 27 mm ³
4	1,905	–	600	2,500	80	14.0	15.4	21.7	Gland: 0.6% Liver: 181 mm ³
5	448	Saturation	390	2,657	88	14.7	14.0	21.0	Gland: 16.5% Kidney: 399 mm ³ Veins: 2 mm ³
6	883	Organ at risk	120	2,230	78	16.8	16.8	24.5	Gland: 5.9% Veins: 86 mm ³
7	1,872	Organ at risk	90	1,875	30	14.7	16.8	22.4	Gland: 3.7% Veins: 98 mm ³
8	2,078	Saturation	540	10,065	75	24.5	25.2	32.2	Gland: 13.8% Gland: 16.5% Liver: 1.1 mm ³
9	1,600	Organ at risk	360	3,141	71	18.2	16.8	21.7	Kidney: 29 mm ³ Gland: 5.3% Kidney: 24 mm ³ Veins: 31 mm ³
10	995	Organ at risk	90	1,553	38	13.3	14.0	20.3	Gland: 3.6% Liver: 997 mm ³
11	2,395	Organ at risk	540	5,823	65	21.7	20.3	28.7	Gland: 2.3% Veins: 1 mm ³
12	995	Organ at risk	60	981	62	12.6	13.3	19.6	Gland: 16.3% Bone: 4 mm ³
13	1,659	–	600	11,328	81	25.2	25.9	34.3	Gland: 8.4%
14	985	Organ at risk	120	3,124	66	19.6	22.4	30.1	
Average	1249 ± 654		293.6 ± 208	3881 ± 3142	70 ± 19	17.6 ± 4.5	18.1 ± 4.3	25.0 ± 4.8	

**Figure 2.** Specific absorption rate in tissues near applicator in (A) radial, and (B), (C) longitudinal (B), (C) slices along the applicator (white space) as well as D) 3D visualization of applicator (blue), tumor (temperature map), kidney (beige), spine (white) and other (purple) with SAR map overlaying tumor volume.

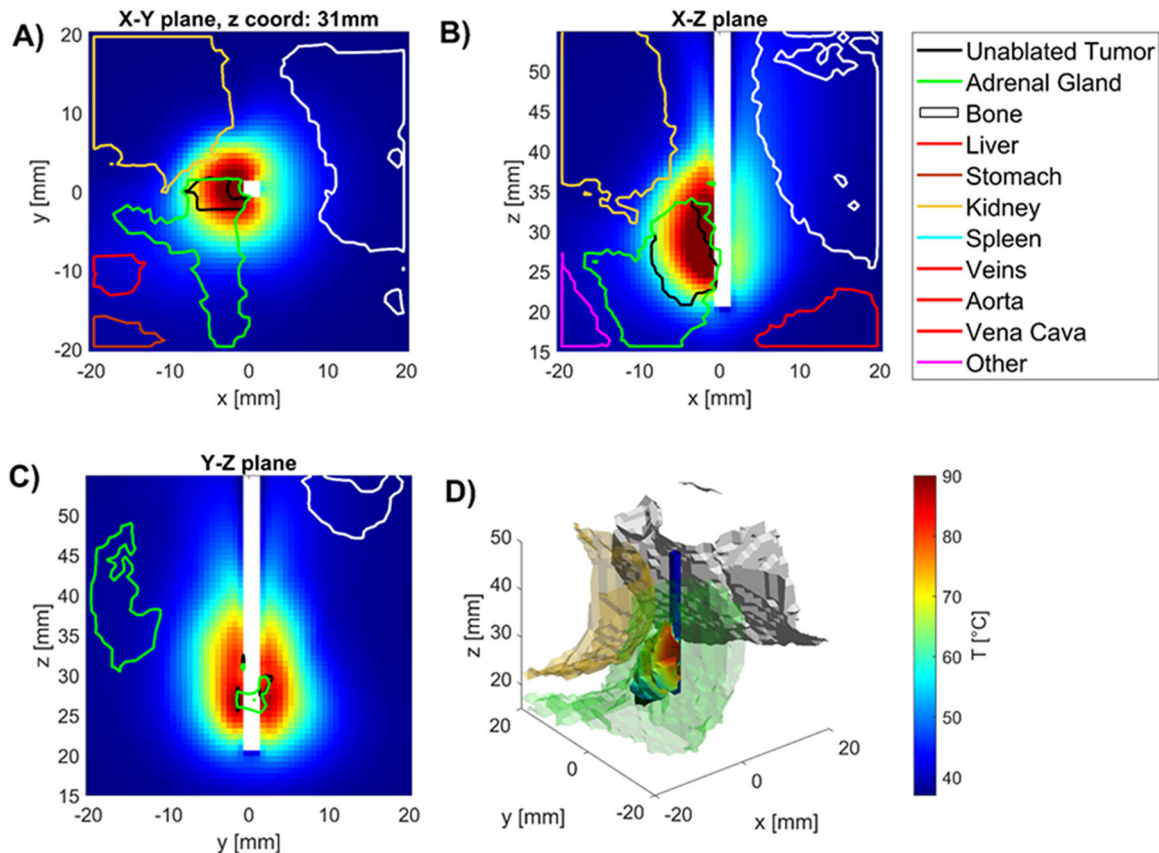


Figure 3. Temperatures in tissues near applicator in (A) radial, and (B), (C) longitudinal (B), (C) slices along the applicator (white space) as well as (D) 3D visualization of applicator (blue), tumor (temperature map), kidney (beige), spine (white) and other (purple) with temperature map overlaying tumor volume.

illustrate that while the microwave power is generally distributed over a suitably large volume relative to the targeted tumor volume, substantial power is absorbed in regions beyond the tumor that are likely to lead to thermal damage to surrounding structures, if no additional thermo-protective measures are employed.

Figure 3 illustrates the temperature profiles around the applicator for case 1 at $t = 270$ s, when the simulated ablation was terminated due to the saturation termination criterion. Temperature maps are displayed in three orthogonal planes; additionally, in the volumetric plot, the temperature map is displayed within regions of the targeted volume where a thermal dose exceeding 240 CEM43 was attained. These images illustrate that ablative heating is generally localized to the target tumor, however, ablative doses do generally extend into the adrenal gland and may affect other adjacent tissue/organs.

For some cases, e.g., case 2, 7, 10, and 12, simulations indicated the ablation should be terminated in under 2 min, due to predicted thermal damage to surrounding structures. Figure 4 illustrates the temperature profile in the targeted tumor and surrounding structures for case 10 at the termination time of $t = 90$ s. It is evident from Figure 4 that the long axis of the ablation zone is almost perpendicular to the axis of the tumor target. Thus, although the volume of tissue ablated is on the order of the target volume, only $\sim 38\%$ of the target volume was ablated before substantial ablative heating occurred in adjacent tissue.

Simulations indicated the sensitivity of applicator positioning relative to the target volume on the predicted ablation

volume. For example, considering case 4, in a pilot simulation, the applicator was positioned 1.5 mm away from the tumor boundary (Figure 5A), with periaudrenal fat between the applicator and the adrenal gland/tumor. This resulted in relatively modest tumor ablation coverage of $\sim 48\%$, impacted by the substantially low dielectric properties of fat which alter the power absorption and resultant thermal profiles. More careful positioning of the ablation applicator adjacent to the adrenal gland (Figure 5B) yielded target tumor coverage of $\sim 79\%$.

Discussion

The present study was undertaken to assess the feasibility of safely delivering targeted thermal ablation to benign aldosterone producing adenomas (APAs) using a previously described 2.45 GHz water-cooled directional MWA applicator. In a prior experimental study, we demonstrated sub-total ablation of normal porcine adrenal gland *in vivo*, with the MWA applicator positioned under open surgery [16]. The ability to thermally spare and preserve functional status of a substantial fraction of the adrenal gland suggested potential for treating patients with bilateral disease, for whom adrenalectomy is precluded. Here, we employed a computational approach, generating 3D patient-specific computational models from diagnostic ^{11}C -metomidate PET/CT scans to simulate MWA of APAs.

The data in Table 3 illustrate that the volume of ablated tissue across all tissue regions ranged between 981 mm^3 and

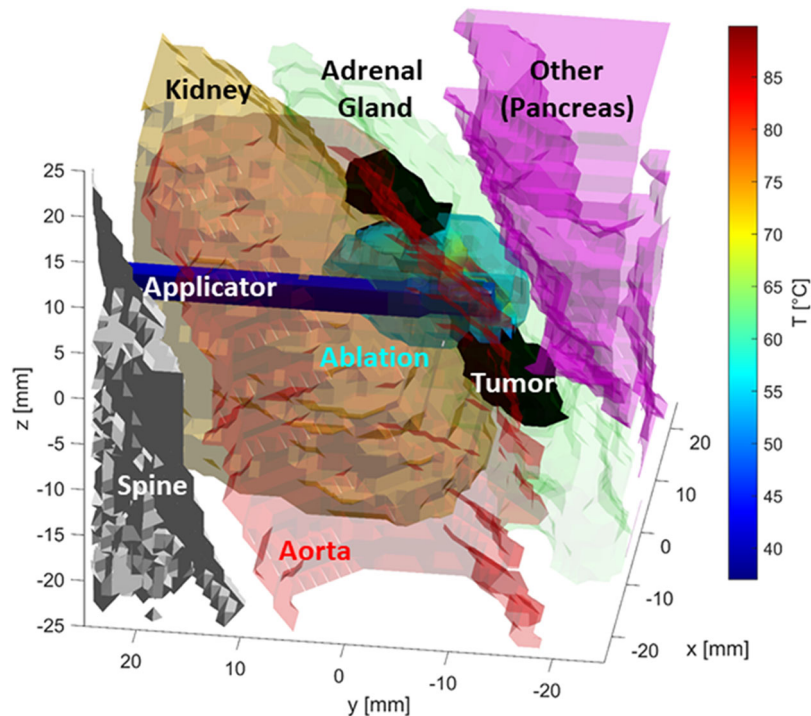


Figure 4. Thermal profiles for case 10 at the termination time of $t = 90$ s. The ablation applicator axis is approximately perpendicular to the long axis of the tumor, resulting in substantial fraction of the ablation zone extending beyond the target in one direction, but lateral extents of the target volume remaining unablated. The ablation duration is limited by unacceptable collateral damage in structures like the adjacent pancreas and intestines (see Table 2).

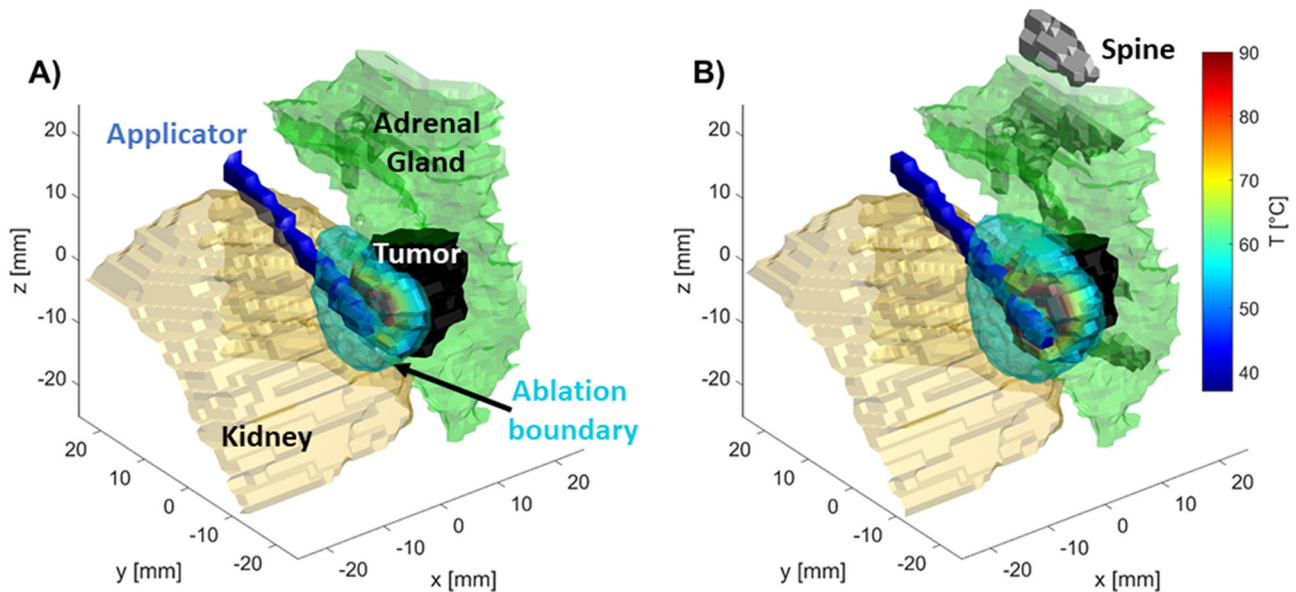


Figure 5. Illustration of the impact of applicator positioning relative to the adrenal gland on thermal profiles. (A) Applicator is approximately 1.5 mm away from the adrenal gland/tumor, separated by a layer of peri-adrenal fat (tumor coverage: $\sim 48\%$) (B) The applicator is adjacent to the adrenal gland/tumor boundary (tumor coverage: $\sim 79\%$).

$11,328 \text{ mm}^3$, exceeding the volume of targeted APAs, which ranged between 393 mm^3 and $2,395 \text{ mm}^3$, in 13/14 cases; the APA volume (995 mm^3) slightly exceeded the ablated tissue volume (981 mm^3) in 1/14 case. Thus, while the ablation applicator seems well suited to creating adequately-sized ablation zone volumes to treat APAs, image-based computational models show that the volume of ablated tissue may not overlap with the targeted APA, thus leaving some unablated residual tumor. Across all considered 14 cases, the average fraction of the APA covered with an ablative thermal

dose was 70%. Importantly, simulations indicated 83.5–96.4% of normal adrenal gland remained below the ablative threshold across all cases, supporting the potential to preserve substantial normal adrenocortical tissue following targeted ablation of APA.

In 4/14 cases, the simulation terminated prior to the maximum simulated ablation duration of 600 s, due to the saturation termination criterion. With the simulated ablation zone growing at less than 1% the growth rate in the first min of ablation, further extending the ablation duration would

present increased thermal damage to non-targeted tissue, with little likelihood of substantially increasing the fraction of APA ablated. When ablating malignant disease with curative intent or for achieving local control, interventionalists aim to ablate the entire tumor and a circumferential margin of normal tissue [52]. For ablation of symptomatic benign disease such as APA, the fraction of the nodule that must be ablated to achieve clinical effect is not well understood. Simulated ablations ran through 10 min in 2/14 cases. In the remaining 6/14 cases, simulations were terminated due to thermal damage to surrounding non-targeted tissue.

Figures 2 to 5 illustrate example power absorption and thermal profiles in select cases (thermal profiles for all 14 cases are provided in the [Supplementary material](#)), and these provide some insights into reasons why 6/14 cases resulted in predicted ablation zones extended over <70% of the targeted APA (range: 38–66%). The most common factor was the position of the ablation applicator axis relative to the major axis of the targeted APA. As illustrated in our prior work [18], the extent of the ablation zone generally ranges between ~25–35 mm along the applicator axis, ~15–18 mm perpendicular to the axis in the direction of maximum power absorption (the ‘forward’ direction), and ~25–35 mm laterally along the other axis perpendicular to the applicator. When the major axis of the APA was not well aligned with the applicator axis (as in [Figure 4](#)), ablation coverage of the targeted APA would be anticipated to be relatively modest. Increasing the duration of ablation, or applied power, for such cases would be unlikely to yield meaningfully improved coverage, as the primary limitation is the orientation of power radiated by the antenna relative to the target. Rather, considering other applicator insertion trajectories and/or repositioning the patient so as to leverage the gravitational effect to achieve a more favorable position of the adrenal gland may provide approaches for better aligning the applicator with the target APA.

Of note, there is no consensus gold standard for patient position for adrenal ablation. Adrenal tumors are most readily accessible *via* a posterior or lateral approach with the patient in an ipsilateral decubitus position. These positions minimize the risk of ipsilateral lung injury and pneumothorax as the lung is hypoinflated [12]. The lateral decubitus position also minimizes the craniocaudal motion of the adrenal gland due to respiration induced diaphragmatic movements. Our computational modeling was based on images acquired in the standard supine position for diagnostic imaging, therefore did not include the gravitational effect of optimal patient position on organs susceptible to thermal damage. Additionally, since our models were developed based on diagnostic imaging scans, the applicator positioning was estimated based on feasible paths for insertion; the impact of applicator insertion on deformation of the APA, adrenal gland, and adjacent soft tissue were not considered. Imaging datasets acquired during interventional procedures with a needle positioned to access the targeted APA (e.g., during ablation or biopsy) may allow for an even more anatomically representative simulation of adrenal ablation. A challenge with image-based modeling of needle/catheter-based

interventional procedures is that the tumor extents may not be as readily visible on interventional imaging, and may be obscured by artifacts due to the interventional tool.

In this computational modeling study, 8/14 simulated ablations were terminated due to thermal damage to surrounding non-target structures exceeding pre-defined tolerable thresholds. In clinical practice, structures around the ablation target can be displaced by the injection of gas/liquid as a thermoprotective measure. Hydrodissection, which involves the infusion of fluid between the target tissue and adjacent structures is a common technique used to protect adjacent structures from thermal damage [53]. This fluid becomes a physical barrier between the target zone of ablation and neighboring tissue. Our models did not include the effect of hydrodissection on structure location when estimating organ thermal exposure damage. Incorporating hydrodissection in computational models of ablation is technically challenging, as the extent of displacement is often operator- and patient-specific, with the volume and rate of infusion of the liquid impacting the barrier size and duration.

Prior studies have demonstrated the impact of peri-adrenal fat on modulating power absorption profiles from microwave ablation antennas [17]. While fat, which has low relative permittivity, generally serves to constrain power toward higher permittivity adrenal/tumor tissue, placement of the ablation applicator such that there is a layer of fat between the applicator and the adrenal gland can substantially diminish the power transferred to the targeted tumor ([Figure 5](#)). Thus, when using an MWA applicator positioned adjacent, rather than within, the targeted APA, accurate placement of the applicator is important to ensure maximal power transfer to the APA for efficient ablation. The use of stereotactic and robotic-assisted positioning of ablation applicators [54] may serve to enhance the accuracy of localized ablation within the targeted APA.

A semi-automated approach was employed to segment targeted APA lesions and surrounding tissues in the present study. Although Artificial intelligence (AI) methods are becoming increasingly utilized in modern healthcare technologies to evaluate medical imagery, there are still several challenges when using such techniques for segmentation and analysis of adrenal and peri-adrenal tissue to facilitate image-based modeling. Segmentation of adrenal glands and adjacent tissue with AI-assisted techniques is technically challenging, due to the adhesion of the adrenal gland with surrounding organs [55]. The proximity of the adrenal glands to abdominal vessels [56] and intra-subject variability in gland size and shape, position and boundaries with adjacent tissue (e.g., liver, spleen, pancreas) present further technical challenges with localization and segmentation of nodules with AI-based methods [57,58]. Further, it has been difficult to establish the robustness and reproducibility of segmenting small adrenal tumors due to the large imbalance between the proportions of foreground and background voxels [57]. There is no established segmentation pipeline or technique for adrenal tumors of various shapes, sizes, and locations [58]. Convolutional Neural Networks (CNN) have been the most preferred method of processing PET/CT image data

due to their feature extraction capabilities and their generalizability across variations in input data. However, a challenge with their use is the requirement of large volumes of data to train the network to ensure accurate segmentation of the adrenal gland adenomas. A further challenge when using this approach is the ability to localize the nodules on intra-procedural imaging, where the environment is dynamic, for example due to the presence of potential deformation caused by applicator insertion. The use of real-time interventional imaging modalities, such as ultrasound, can be used to assist this, where innovative modeling techniques require to be explored suited for processing such time dependent data. Biologically-inspired AI techniques such as Spiking Neural Networks (SNN) have had success in classification problems with similar time-varying data, however with less accuracy using static images. To address this segmentation challenge may require more than one AI technique that can exploit both intra-procedural and pre-procedural imaging data. For example, a committee-system of a CNN with diagnostic pre-procedural scan (PET/CT) data and SNNs with real-time intra-procedural imaging data, could provide increased accuracy or confidence in the segmentation decision. This approach sets the focus of our future work in addressing the adrenal segmentation challenge.

We note that this study considered only a single applied power level (80W), similar to power settings used in our prior experimental studies with the directional water-cooled MWA applicator [16,18]. Consideration of other applied power level/ablation duration combinations may provide more degrees of freedom for achieving ablation more localized to the targeted tissue. Further, this study only considered one applicator position relative. For irregularly shaped targets, where the extents of the target are not relatively well matched in orthogonal axes, it may be appropriate to translate and reposition the applicator so as to better cover the target volume, as is performed for some thyroid ablation procedures [59].

Conclusion

We developed patient-specific computational models of microwave ablation of benign adrenal tumor targets for a 14-patient dataset of diagnostic PET/CT scans. Across the 14 patients, adrenal tumor volumes ranged between 393 mm³ and 2,395 mm³; cumulative volume of ablated tissue predicted by simulations, including both target and non-target tissue, ranged between 981 mm³ and 11,328 mm³, indicating the importance of positioning and aligning the ablation applicator with the targeted tumor. On average, 70% of the adrenal tumor volumes could be heated to an ablative thermal dose of 240CEM43, while limiting thermal damage to non-target structures and thermally sparing 83.5–96.4% of normal adrenal gland. Simulations considered rate of growth of the ablation zone and tolerable thermal damage to surrounding structures for constraining the ablation duration; the average ablation duration was 293 s (range: 60–600 s). Consideration of thermoprotective measures such as hydro-dissection and patient positioning so as to favorably orient

the adrenal gland relative to the applicator may allow for even greater coverage of the target volume with an ablative thermal dose.

Disclosure statement

Punit Prakash discloses receiving royalties from KSU Research Foundation for licensed patents on ablation technologies.

Funding

This work was supported by the National Institutes of Health grant R01EB028848, Science Foundation Ireland (SFI) 20/US/3676, HSC R&D - STL/5521/19 and UKRI MRC - MC_PC.20021.

ORCID

Jan Sebek  <http://orcid.org/0000-0002-2116-6697>
Mark Gurnell  <http://orcid.org/0000-0001-5745-6832>
Punit Prakash  <http://orcid.org/0000-0001-6467-722X>

References

- [1] Mulatero P, Stowasser M, Loh K-C, et al. Increased diagnosis of primary aldosteronism, including surgically correctable forms, in centers from five continents. *J Clin Endocrinol Metab.* 2004;89(3):1045–1050.
- [2] Rossi GP, Bernini G, Caliumi C, et al. A prospective study of the prevalence of primary aldosteronism in 1,125 hypertensive patients. *J Am Coll Cardiol.* 2006;48(11):2293–2300.
- [3] Young WF. Primary aldosteronism: renaissance of a syndrome. *Clin Endocrinol.* 2007;66(5):607–618.
- [4] Funder J. Primary aldosteronism: treatment of the disease, and new therapeutic approaches. *Best Pract Res Clin Endocrinol Metab.* 2020;34(2):101368.
- [5] Nishimura M, Uzu T, Fujii T, et al. Cardiovascular complications in patients with primary aldosteronism. *Am J Kidney Dis.* 1999;33(2):261–266.
- [6] Mulatero P, Monticone S, Bertello C, et al. Long-term cardio- and cerebrovascular events in patients with primary aldosteronism. *J Clin Endocrinol Metab.* 2013;98(12):4826–4833.
- [7] Rossi GP, Funder JW. Adrenal vein sampling is the preferred method to select patients with primary aldosteronism for adrenalectomy: pro side of the argument. *Hypertension.* 2018;71(1):5–9.
- [8] Funder JW, Carey RM, Fardella C, et al. Case detection, diagnosis, and treatment of patients with primary aldosteronism: an endocrine society clinical practice guideline. *J Clin Endocrinol Metab.* 2008;93(9):3266–3281.
- [9] Karashima S, Yoneda T, Kometani M, et al. Comparison of eplerenone and spironolactone for the treatment of primary aldosteronism. *Hypertens Res.* 2016;39(3):133–137.
- [10] Donlon P, Dennedy MC. Thermal ablation in adrenal disorders: a discussion of the technology, the clinical evidence and the future. *Curr Opin Endocrinol Diabetes Obes.* 2021;28(3):291–302.
- [11] Zheng L, Zhou F, Yu X, et al. Hypertensive crisis during microwave ablation of adrenal neoplasms: a retrospective analysis of predictive factors. *J Vasc Interv Radiol.* 2019;30(9):1343–1350.
- [12] Venkatesan AM, Locklin J, Dupuy DE, et al. Percutaneous ablation of adrenal tumors. *Tech Vasc Interv Radiol.* 2010;13(2):89–99.
- [13] Ren C, Liang P, Yu X, et al. Percutaneous microwave ablation of adrenal tumours under ultrasound guidance in 33 patients with 35 tumours: a single-centre experience. *Int J Hyperthermia.* 2016;32(5):517–523.
- [14] Yang M-H, Tyan Y-S, Huang Y-H, et al. Comparison of radiofrequency ablation versus laparoscopic adrenalectomy for benign

- aldosterone-producing adenoma. *Radiol Med*. 2016;121(10): 811–819.
- [15] Liu SY, Chu CM, Kong AP, et al. Radiofrequency ablation compared with laparoscopic adrenalectomy for aldosterone-producing adenoma. *Br J Surg*. 2016;103(11):1476–1486.
- [16] Donlon PT, Fallahi H, Beard WL, et al. Using microwave thermal ablation to develop a subtotal, cortical-sparing approach to the management of primary aldosteronism. *Int J Hyperthermia*. 2019; 36(1):904–913.
- [17] Bottiglieri A, Ruvio G, O'Halloran M, et al. Exploiting tissue dielectric properties to shape microwave thermal ablation zones. *Sensors*. 2020;20(14):3960.
- [18] Sebek J, Curto S, Bortel R, et al. Analysis of minimally invasive directional antennas for microwave tissue ablation. *Int J Hyperthermia*. 2017;33(1):51–60.
- [19] Pfannenstiel A, Sebek J, Fallahi H, et al. Directional microwave ablation: experimental evaluation of a 2.45-GHz applicator in *ex vivo* and *in vivo* liver. *J Vasc Interv Radiol*. 2020;31(7): 1170–1177.e2.
- [20] Pfannenstiel A, Iannuccilli J, Cornelis FH, et al. Shaping the future of microwave tumor ablation: a new direction in precision and control of device performance. *Int J Hyperthermia*. 2022;39(1): 664–674.
- [21] Liu D, Adams MS, Diederich CJ. Endobronchial high-intensity ultrasound for thermal therapy of pulmonary malignancies: simulations with patient-specific lung models. *Int J Hyperthermia*. 2019;36(1):1107–1120.
- [22] Sebek J, Taeprasartsit P, Wibowo H, et al. Microwave ablation of lung tumors: a probabilistic approach for simulation-based treatment planning. *Med Phys*. 2021;48(7):3991–4003.
- [23] Wang Z, Aarya I, Gueorguieva M, et al. Image-based 3D modeling and validation of radiofrequency interstitial tumor ablation using a tissue-mimicking breast phantom. *Int J Comput Assist Radiol Surg*. 2012;7(6):941–948.
- [24] Yeniaras E, Fuentes DT, Fahrenholtz SJ, et al. Design and initial evaluation of a treatment planning software system for MRI-guided laser ablation in the brain. *Int J Comput Assist Radiol Surg*. 2014;9(4):659–667.
- [25] Funder JW, Carey RM, Mantero F, et al. The management of primary aldosteronism: case detection, diagnosis, and treatment: an endocrine society clinical practice guideline. *J Clin Endocrinol Metab*. 2016;101(5):1889–1916.
- [26] Browne GA, Griffin TP, O'Shea PM, et al. β -Blocker withdrawal is preferable for accurate interpretation of the aldosterone-renin ratio in chronically treated hypertension. *Clin Endocrinol*. 2016; 84(3):325–331.
- [27] Ahmed AH, Cowley D, Wolley M, et al. Seated saline suppression testing for the diagnosis of primary aldosteronism: a preliminary study. *J Clin Endocrinol Metab*. 2014;99(8):2745–2753.
- [28] Burton TJ, Mackenzie IS, Balan K, et al. Evaluation of the sensitivity and specificity of (11)C-metomidate positron emission tomography (PET)-CT for lateralizing aldosterone secretion by conn's adenomas. *J Clin Endocrinol Metab*. 2012;97(1):100–109.
- [29] O'Shea PM, O'Donoghue D, Bashari W, et al. Metomidate PET/CT is a useful adjunct for lateralization of primary aldosteronism in routine clinical practice. *Clin Endocrinol*. 2019;90(5):670–679.
- [30] Almekkawy M, Chen J, Ellis MD, et al. Therapeutic systems and technologies: state-of-the-art applications, opportunities, and challenges. *IEEE Rev Biomed Eng*. 2020;13:325–339.
- [31] McWilliams BT, Schnell EE, Curto S, et al. A directional interstitial antenna for microwave tissue ablation: theoretical and experimental investigation. *IEEE Trans Biomed Eng*. 2015;62(9): 2144–2150.
- [32] Cavagnaro M, Amabile C, Bernardi P, et al. A minimally invasive antenna for microwave ablation therapies: design, performances, and experimental assessment. *IEEE Trans Biomed Eng*. 2011;58(4): 949–959.
- [33] Mohtashami Y, Luyen H, Hagness SC, et al. Non-coaxial-based microwave ablation antennas for creating symmetric and asymmetric coagulation zones. *J Appl Phys*. 2018;123(21):214903.
- [34] Hessinger C, Schüßler M, Klos S, et al. Numerical optimization of an open-ended coaxial slot applicator for the detection and microwave ablation of tumors. *Biology*. 2021;10(9):914.
- [35] Fallahi H, Clausning D, Shahzad A, et al. Microwave antennas for thermal ablation of benign adrenal adenomas. *Biomed. Phys. Eng. Express*. 2019;5(2):025044.
- [36] Adams MS, Scott SJ, Salgaonkar VA, et al. Thermal therapy of pancreatic tumours using endoluminal ultrasound: parametric and patient-specific modelling. *Int J Hyperthermia*. 2016;32(2): 97–111.
- [37] Scott SJ, Salgaonkar V, Prakash P, et al. Interstitial ultrasound ablation of vertebral and paraspinal tumours: parametric and patient-specific simulations. *Int J Hyperthermia*. 2014;30(4): 228–244.
- [38] Faridi P, Keselman P, Fallahi H, et al. Experimental assessment of microwave ablation computational modeling with MR thermometry. *Med Phys*. 2020;47(9):3777–3788.
- [39] Pennes HH. Analysis of tissue and arterial blood temperatures in the resting human forearm. *J Appl Physiol*. 1948;1(2):93–122.
- [40] IT'IS Foundation. Tissue Properties Database V4.0 [Internet]. IT'IS Foundation. 2018; [cited 2021 Mar 19]. Available from <https://www.itis.ethz.ch/virtual-population/tissue-properties/downloads/database-v4-0/>.
- [41] Bottiglieri A, Shahzad A, Donlon P, et al. Dielectric characterization of *ex vivo* ovine and human adrenal glands for microwave thermal ablation applications. *IEEE J. Electromagn. RF Microw. Med. Biol*. 2021;5(3):254–261.
- [42] McIntosh RL, Anderson V. A comprehensive tissue properties database provided for the thermal assessment of a human at rest. *Biophys. Rev. Lett*. 2010;05(03):129–151.
- [43] Sebek J, Albin N, Bortel R, et al. Sensitivity of microwave ablation models to tissue biophysical properties: a first step toward probabilistic modeling and treatment planning. *Med Phys*. 2016;43(5): 2649–2661.
- [44] Fallahi H, Sebek J, Prakash P. Broadband dielectric properties of *ex vivo* bovine liver tissue characterized at ablative temperatures. *IEEE Trans Biomed Eng*. 2021;68(1):90–98.
- [45] Hall SK, Ooi EH, Payne SJ. Cell death, perfusion and electrical parameters are critical in models of hepatic radiofrequency ablation. *Int J Hyperthermia*. 2015;31(5):538–550.
- [46] Pearce JA. Models for thermal damage in tissues: processes and applications. *Crit Rev Biomed Eng*. 2010;38(1):1–20.
- [47] Bing C, Patel P, Staruch RM, et al. Longer heating duration increases localized doxorubicin deposition and therapeutic index in Vx2 tumors using MR-HIFU mild hyperthermia and thermosensitive liposomal doxorubicin. *Int J Hyperthermia*. 2019;36(1): 195–202.
- [48] Wijlemans JW, Bartels LW, Deckers R, et al. Magnetic resonance-guided high-intensity focused ultrasound (MR-HIFU) ablation of liver tumours. *Cancer Imaging*. 2012;12:387–394.
- [49] Quesson B, Laurent C, Maclair G, et al. Real-time volumetric MRI thermometry of focused ultrasound ablation *in vivo*: a feasibility study in pig liver and kidney. *NMR Biomed*. 2011;24(2):145–153.
- [50] Hijnen: Thermal combination therapies for local drug... – Google Scholar [Internet]; [cited 2022 Aug 24]. Available from https://scholar.google.com/scholar_lookup?hl=en&volume=114&publication_year=2017&pages=E4802-e4811&author=N+Hijnen&author=E+Kneepkens&author=M+de+Smet&title=Thermal+combination+therapies+for+local+drug+delivery+by+magnetic+resonance-guided+high-intensity+focused+ultrasound.
- [51] Kaye EA, Cornelis FH, Petre EN, et al. Volumetric 3D assessment of ablation zones after thermal ablation of colorectal liver metastases to improve prediction of local tumor progression. *Eur Radiol*. 2019;29(5):2698–2705.
- [52] Sandu R-M, Paolucci I, Ruiter SJS, et al. Volumetric quantitative ablation margins for assessment of ablation completeness in thermal ablation of liver tumors. *Front Oncol*. 2021;11:623098.
- [53] Campbell C, Lubner MG, Hinshaw JL, et al. Contrast media-doped hydrodissection during thermal ablation: optimizing contrast

- media concentration for improved visibility on CT images. *AJR Am J Roentgenol.* [2012](#);199(3):677–682.
- [54] Tinguely P, Paolucci I, Ruiter SJS, et al. Stereotactic and robotic minimally invasive thermal ablation of malignant liver tumors: a systematic review and Meta-Analysis. *Front Oncol.* [2021](#);11:713685.
- [55] Zhang G, Li Z. An adrenal segmentation model based on shape associating level set in sequence of CT images. *J Sign Process Syst.* [2019](#);91(10):1169–1177.
- [56] Zhao W, He H, Zhao J, et al. Adrenal tumor vessels segmentation using convolutional neural network in computed tomography angiography. *Annu Int Conf IEEE Eng Med Biol Soc.* [2019](#);2019:1006–1009.
- [57] Luo G, Yang Q, Chen T, et al. An optimized two-stage cascaded deep neural network for adrenal segmentation on CT images. *Comput Biol Med.* [2021](#);136:104749.
- [58] Koyuncu H, Ceylan R, Erdogan H, et al. A novel pipeline for adrenal tumour segmentation. *Comput Methods Programs Biomed.* [2018](#);159:77–86.
- [59] Souza K d, Rahal A, Volpi EM, et al. Hydrodissection and programmed stop sedation in 100% of benign thyroid nodules treated with radiofrequency ablation. *Eur J Radiol.* [2020](#);133:109354.